

# Planar Optical Waveguides Using Poly(styrene-ethylene-butylene-styrene) Activated with Inorganic Lead Halide Perovskite Nanoplates

Tsafir Abir, Reut Shechter, Tal Ellenbogen, and Yehonadav Bekenstein\*



Cite This: *ACS Photonics* 2020, 7, 2329–2336



Read Online

ACCESS |



Metrics & More



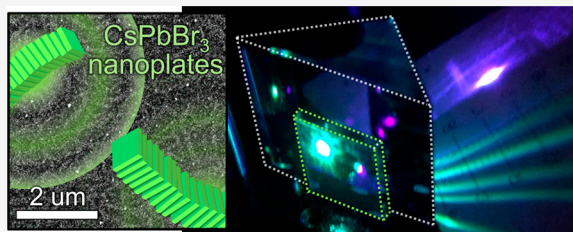
Article Recommendations



Supporting Information

**ABSTRACT:** Lead halide perovskite nanoplates support strongly quantum confined excitons, high photoluminescence quantum yield, fast and narrow photoluminescence spectra. Future use of these nanomaterials is strongly dependent on the ability to enhance their stability and engineer the out-coupling of excitonic emission. Optical waveguides can harness their attractive optical properties enabling integration into photonic devices and preventing degradation. In this study we activate planar polymer waveguides of poly(styrene-ethylene-butylene-styrene) with colloidal synthesized CsPbBr<sub>3</sub> nanoplates and study interactions between perovskite confined excitons and the optical waveguide modes. Beyond optical engineering, the polymer forming the waveguide serves also to encapsulate the perovskite nanocrystals, protecting them from the environment. Angle-dependent photoluminescence measurements indicate coupling between the quantum confined excitons in the nanoplates and the planar guided modes. This is evident by the emission of photons with momenta and polarization states matching those of the guided modes. We achieve an order of magnitude shortening of the emission lifetime via Purcell effect. Achieving fast emission from perovskite nanoplate activated waveguides is of interest in the context of searching for an efficient and coherent single photon source. These findings can serve as a first engineering step in the direction for a more complex nanoperoovskite waveguide based photonic structure.

**KEYWORDS:** colloidal nanocrystals, Purcell effect, confined excitons, oriented emission, weak coupling



Lead halide perovskites (LHPs) are direct band gap semiconductors that possess intriguing optical and electronic properties.<sup>1</sup> The focus on LHPs began a few decades ago with studies of organic–inorganic hybrid thin films in field-effect transistors,<sup>2</sup> and rapidly evolved to their use as highly efficient absorbing layers in photovoltaic cells<sup>3</sup> and light-emitting diodes.<sup>4,5</sup> More recently, motivated due to several attractive physical aspects, the studies of LHPs expanded to the field of colloidal nanocrystals (NCs).<sup>6–8</sup> The ionic nature of LHPs enables growth of perovskite nanocrystals with good optical properties at low temperatures and in ambient conditions. Additionally, it is possible to modify and enhance their absorption and emission properties by controlling their size, shape, and halide composition.<sup>9</sup> Moreover, in contrast to traditional semiconductor NCs that require a protective shell to shield the exciton from surface traps, LHPs have shown to reach near unity quantum yield without such a shell. The lack of a wide band gap shell positions them as attractive luminescent nanocrystals that are easily processed and with lower resistivity for electroluminescence charge injection.<sup>10</sup> Despite these appealing properties for optoelectronics, a major drawback of LHP NCs is their relatively low stability. The ionic characteristics of the atomic bonds in LHP, which are responsible for some of

their special properties, also render the NCs' structure more labile. One approach that has been demonstrated recently is to use CVD grown nanowires and nanoplates<sup>11,12</sup> (NPLs) on the order of microns and hundreds of nanometers for photonic applications.<sup>13,14</sup> Such crystals have shown to be stable enough to withstand significant excitation cycles and demonstrated spontaneous emission and lasing.<sup>15,16</sup> Another approach is to embed the NCs in a protective material such as glass<sup>17</sup> or polymers<sup>18</sup> and isolate them from oxygen and moisture.

In this study we chose to work with fully inorganic LHPs,<sup>6</sup> where typically large Cs<sup>+</sup> cations replace the small organic molecules of the organic–inorganic hybrids (Figure 1a inset); all inorganic halide perovskites have higher crystal melting temperatures and present better stability. Recent use of inorganic LHP NCs in optoelectronic devices includes their incorporation as both active layers of light-emitting

Received: March 26, 2020

Published: August 7, 2020



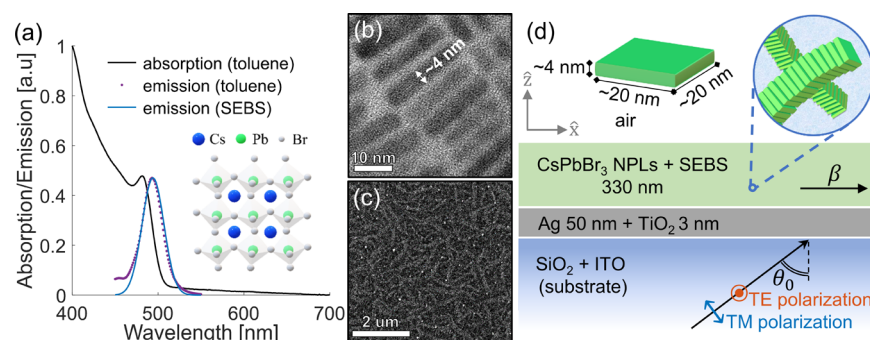


**Figure 1.** (a) Optical absorption and emission spectra for NPLs. Crystal structure of orthorhombic CsPbBr<sub>3</sub> (inset). (b) HRTEM image of stacked perovskite NPLs as viewed from their narrow side, where their thickness of  $\sim 4$  nm can be measured. (c) SEM image of the planar wave guides showing columns of the stacked NPLs in SEBS aligned in plane with the waveguiding layer. (d) Illustration depicting 4–5 unit cells thick NPL dimensions and stacking within the waveguiding layer. Schematic description of the fabricated waveguide, incidents light of the reflection measurements and the polarization directions, where the ITO serves as an adhesive layer between the SiO<sub>2</sub> and Ag layers. The TiO<sub>2</sub> thin film separates and protects the silver from above.

diodes<sup>19–21</sup> and absorbing layers in photovoltaic cells.<sup>22,23</sup> Low-threshold amplified spontaneous emission and lasing from experimental systems, where LHP NCs perform as a gain medium, have been reported.<sup>24,25</sup> The fast emission rate attributed to the bright triplet excitonic states in LHP NCs<sup>26</sup> motivated the use of individual NCs as a single-photon source<sup>27</sup> even at room temperature.<sup>28</sup> Moreover, the generation of indistinguishable entangled photon pairs for quantum information processing was also reported.<sup>29</sup> Previous studies of optical waveguiding and LHP NCs include LHP nanowires that were shown to support guided waves and were used to make detectors<sup>30–32</sup> and lasers.<sup>33–35</sup> Thin films of LHPs were integrated and shaped in waveguiding platforms to produce detectors,<sup>36</sup> amplifiers,<sup>36,37</sup> and lasers.<sup>38,39</sup> In all these experiments the LHP crystals used were orders of magnitude larger than the exciton's Bohr radius (7 nm in CsPbBr<sub>3</sub>); therefore, quantum confined excitons were eluded.

Here we present a study of CsPbBr<sub>3</sub> NCs in a NPL morphology in which the excitons are strongly quantum confined. The NPLs have been integrated into a polymer-based asymmetric planar optical waveguide. The system is interesting since on one hand the exciton binding energy can be synthetically controlled via reducing the thickness of NPLs resulting in strongly quantum confined exciton.<sup>40</sup> On the other hand, waveguides support macroscopic propagating optical modes which interact with the aforementioned excitons enabling photonic manipulation. In this study we selected the planar waveguide geometry due to ease of fabrication and characterization. However, the ideas are general and can be expanded to other waveguiding geometries.

The polymer component of the system serves two purposes: first, to form the waveguiding dielectric slab and, second, to encapsulate and protect the NCs from moisture and oxygen.<sup>18</sup> Previous studies by us and others have shown that for perovskite encapsulation not all polymers are equal.<sup>18</sup> Rainò et al.<sup>41</sup> demonstrated that counterintuitively it is not the overall water permeability of a polymer that is correlated with the observed perovskite nanocrystals stabilities. The interfaces formed between the polymer matrices and the NC surfaces which are covered with alkyl chain ligands play a major role. In the commonly used poly(methyl methacrylate) (PMMA), only partial coverage of the NCs surface is achieved due to poor NCs–polymer interaction, which is assigned to the presence of polar ester groups in the PMMA. For hydrophobic polymers

such as polystyrene and poly(styrene-ethylene-butylene-styrene) (SEBS) which are more compatible with the highly hydrophobic ligands on the NCs surfaces, a better interface, and therefore encapsulation, is achieved, resulting in the long-term stability of the encapsulated NCs in the polymer matrix.

Here this work departs from other studies, as we selected SEBS which is a low-cost triblock copolymer that combines high formability and recyclability with high toughness. SEBS is mechanically highly ductile and therefore superior to polystyrene since it enables processing into thick samples with effectively zero cracking defects that form optically clear matrices which are critical for high quality waveguides and optical devices.

In the proceeding sections we present the design and fabrication of planar waveguide activated with LHP NPLs. Optical characterization of the fabricated sample together with details about the experimental setup are discussed. Additionally, we present numerical calculations used for the evaluation of the optical response and the identification of the modes interacting with the NPLs' excitons. Finally, we examined the lifetime of the modified emission to further assess the interaction.

NPL NCs were colloiddally synthesized using the method previously reported by Bekenstein et al.<sup>9</sup> (see [Methods](#) for details). Post-synthesis the NPLs were cleaned and dispersed in toluene for characterization and further processing. The stoichiometry of a finite thickness LHP NPL is determined by the composition of the crystal facets. Here we assume a bromide surface termination following work of Weidman et al. and stoichiometries of [CsPbBr<sub>3</sub>]<sub>*n*-1</sub>PbBr<sub>4</sub>, where *n* is the number of unit cells.<sup>40</sup> Transmission electron microscopy (TEM) depicts the anisotropic shapes of the NPLs with lateral dimensions of  $\sim 20$  nm and thicknesses of  $\sim 4$  nm (Figure 1b). These dimensions can be assigned to 4–5 perovskite unit cells according to a previous report<sup>9</sup> which also agrees with the absorption and emission spectrum presented in Figure 1a. The peak of the NPL photoluminescence emission was measured to be at a wavelength of  $\sim 488$  nm, as shown by the dotted line in Figure 1a. The anisotropic shape of the plates favors face-to-face stacking and assemblies into columnar structures extending microns in length (Figure 1b). This has been previously observed on slowly dried samples,<sup>9</sup> and in this work we see similar structures even when quickly dried in SEBS mixtures.

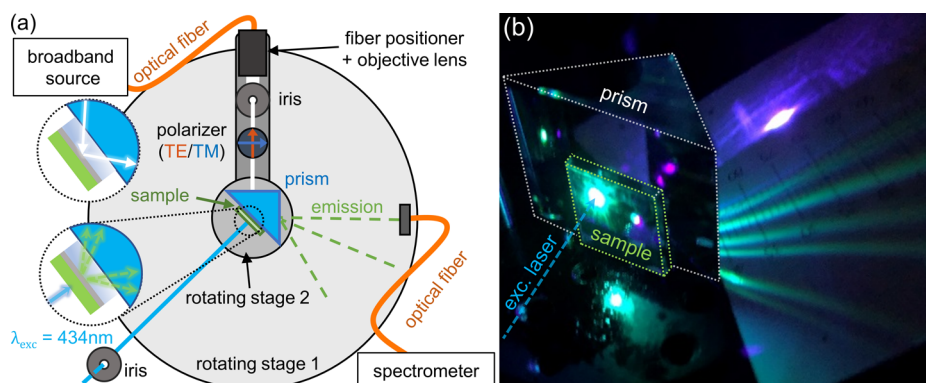


**Figure 2.** (a) Illustration of the measurement setup (details of the components used can be found in the main text). The white lines refer to the broad-band source (used for the reflection measurements), blue line indicated the excitation laser, and the dashed green lines represent the emission (only relevant in emission measurements). The interior of the small dotted circles represents a closeup to clarify the illumination direction in the reflection/emission (top/bottom circle respectively) measurement. (b) Image of a waveguiding sample mounted on the prism and of emission leaking from the waveguide, through the prism onto a viewing card. The dotted white/green lines mark the contour of the prism/sample, and the dashed blue arrow represents the excitation laser.

The waveguide is formed by spin-casting a mixed solution of NPLs in SEBS dissolved in toluene, on top of a 50 nm thick silver layer (see [Methods](#) section for details). The thickness of the resulting dielectric slab was measured to be  $330 \pm 20$  nm, and the total layout of the waveguide is illustrated in [Figure 1d](#). SEM characterization of the NPL activated waveguides shows the self-assembled NPL columns with in-plane horizontally orientation ([Figure 1c](#)). This ordering forces the NPL narrow dimension to favor the orientation parallel to the guided modes' propagation. Confinement of light to the wave-guiding layer is carried out by total internal reflection at the layer's interface with the air, and by partial reflection from the silver film. While the radiation loss through the silver layer reduces the quality factor of the waveguide, this configuration allows prism-based in- and out-coupling of light through the substrate (using a Kretschmann geometry-based setup [Figure 2](#)).

The initial experimental characterization is divided into two parts. The first consists of angle-resolved emission measurements of the NPLs from the photonic waveguide. In the second, a characterization of waveguide modes' dispersion was performed by angle- and polarization-resolved reflection measurements. A schematic description of the experimental setup is illustrated in [Figure 2a](#). As previously mentioned, the waveguide requires steep incidence angles, above the critical angle of the glass–air interface. This can be achieved by mounting the sample on a right-angle prism (Thorlabs, PS908 N-BK7, uncoated). Additionally, the bottom of the glass substrate has been applied with immersion oil, to enable impedance matching and efficient bidirectional light transfer with the prism and provide efficient means for measuring the sample.

The NPL excitation was done nonresonantly ( $\lambda_{exc} = 434$  nm), at normal incidence and through the air interface using a femtosecond laser (Coherent, Chameleon Ultra and Chameleon compact OPO-Vis). The emission from the sample was observed to leak out through the silver and the prism at specific angles as seen in [Figure 2b](#). The emitted light from the sample was collected by an optical fiber held on rotating stage 1 enabling measurement of the angle dependent emission. The other end of the fiber directed the emitted light into a spectrometer (Andor, Shamrock 193i spectrograph and Newton EMCCD camera). The excitonic emission spectra were measured (blue line in [Figure 1a](#)) and the peak emission

was found at a wavelength of 494 nm (green dashed line), slightly red-shifted compared to NPLs dispersed in toluene (488 nm). This red shift can be attributed to the change in the NPLs' dielectric environment. [Figure 3a](#) shows the emission spectra from the waveguide, at different collection angles. The cross section of this emission spectra at 494 nm is plotted at the bottom of [Figure 3a](#) (green line) to emphasize the sharp increase in the emission at specific angles.

Reflection measurements were performed to investigate the nature of the angle-dependent emission and to reveal the optical guided modes' dispersion. A visible broad-band source (Newport, Xenon arc lamp in 67005 housing) was coupled to an optical fiber and was directed and collimated by a fiber positioner (Newport, 9091) and an objective lens (Newport, M-10X, 0.25NA). A polarizer (Thorlabs, WP25M-VIS) and an iris were used to selectively excite the transverse electric (TE) or the transverse magnetic (TM) modes at the same excitation spot as in the emission measurements. For the reflection measurements the incident angle was adjusted using rotating stage 2 on which the prism with the sample were mounted. The reflected light was collected using a fiber as done in the emission measurements.

When the parallel momentum component of incident light matches that of a guided mode ( $\beta$ ), light is efficiently coupled into the waveguide and a dip in the reflection spectrum appears. This condition is described by

$$\beta = n_{BK7} \frac{2\pi}{\lambda} \sin \theta \quad (1)$$

where  $n_{BK7}$  is the refractive index of the glass substrate that was used (N-BK7),  $\lambda$  is the incident light's wavelength in free space, and  $\theta$  is the angle of incidence. Thus, by measuring the reflectance at different incidence angles the guided modes' dispersion can be revealed. By depicting the ratio between reflection spectra of the two polarizations, one can present the measured dispersion for both TE and TM modes in a single graph ([Figure 3b](#)), where TE modes appear as peaks and TM modes as dips. [Figures 3a,b](#) provide a comparison between the angle-resolved reflection and emission spectra, which clearly indicates an increase in the emission when the LHP NPL excitonic emission overlaps with a guided mode (in resonance).

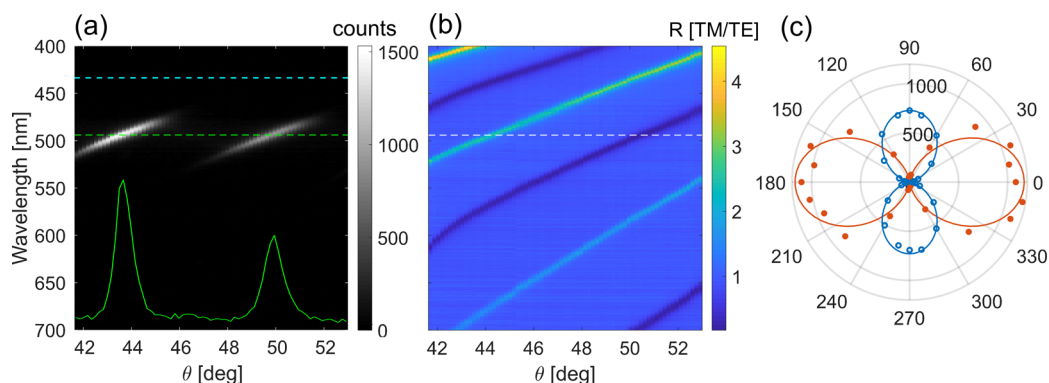


**Figure 3.** (a) Emission measured from the waveguide at different collection angles and (b) normalized reflection (TM/TE) for different incident angles. The wavelength scale is identical in (a) and (b). The white and green dashed lines represent the exciton's emission peak (494 nm) and the cyan dashed line shows the wavelength of the excitation laser (434 nm). The green line represents the angle dependent photon count at a wavelength of 494 nm. (c) Polarization measurements of the emission. The orange points show the measured emission coupled to TE mode (at  $\theta = 43.5^\circ$ ) and the blue circles the emission coupled to TM mode (at  $\theta = 49.9^\circ$ ), while the curved lines represent ideal linear polarization.

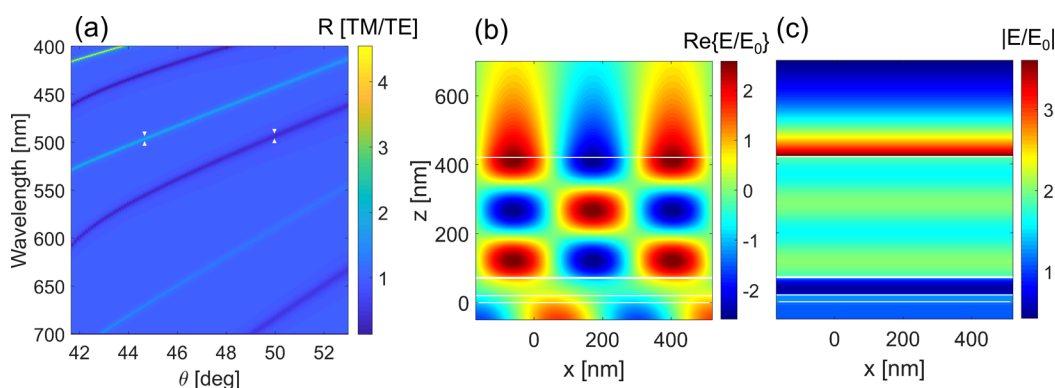


**Figure 4.** (a) Calculated normalized reflection (TM/TE) from the waveguide. (b)  $TE_2$  mode profile for  $\lambda = 497$  nm at  $\theta = 43.4^\circ$  and (c)  $TM_1$  mode profile for  $\lambda = 499$  nm at  $\theta = 50.1^\circ$ , marked by the white arrows in (a). The  $x$  and  $z$  axes refer to the same direction as mentioned in Figure 1d. The  $z$  axis is identical for both figures. The white lines mark the layers' interfaces.

By comparing the emission with the reflection measurements (Figure 3a,b), we demonstrate that NPLs placed in an optical waveguide emit photons predominantly with momentum matching that of guided modes. This is apparent since when the excitons are in resonance with the guided modes, the emission is 15 and 12 times brighter, for the TE and TM modes, respectively (compared to background emission measured at off-resonance angles). Unfortunately, we cannot assign the difference in TE/TM emission intensities to coupling strength of the NPL exciton to the different modes. This is for two reasons: (a) Indeed, the exciton dipole moment is fixed in plane of NPLs, but since the assembled stacked plates orientation varies in the planar waveguides, both TE/TM modes may be coupled similarly. (b) Increasing the collection angle results in a consistent reduction in the emission (due to a decrease in leakage efficiency out of the waveguide and/or a decrease in coupling strength), which affects the TE/TM emission that is measured in different angles. From comparison of the emission of photons with momentum values matching  $\beta$  to photons which are not, we discovered that about 2/3 of the total amount of photons are emitted to the guided modes. Additionally, analysis of the emitted photons' polarization is presented in Figure 3c. At resonance angles,  $43.5^\circ$  and  $49.9^\circ$ , we find the emitted photons to be 95% and 92% linearly polarized in accordance with the TE and TM modes (respectively) they are coupled with.

The results presented in Figure 3 show clear coupling of the excitons to the optical guided modes. To identify the specific interacting guided modes, we modeled the optical response of the waveguide using a method introduced by Ohta and Ishida.<sup>42</sup> For the model we used the waveguide's dimensions as specified in Figure 1d, with frequency-dependent refractive indices ( $n$ ) and extinction coefficients ( $k$ ) of each of the comprising materials.  $n$  and  $\kappa$  for the polymer–NPL layer remain variables of the models which we wish to evaluate. Comparison between the calculated reflection from the stratified layers presented in Figure 4a to the experimental results in Figure 3b enabled the evaluation of the effective refractive index and extinction coefficient of the composite wave-guiding layer. They were found to be  $n = 1.66 \pm 0.151$  and  $\kappa = 0.008 \pm 0.002$ , with the variations related to the frequency dependence. We used these parameters to calculate the complex electric field amplitudes within the different layers and constructed the modes' profiles. These mode profiles are sampled by selecting the wavevectors and polarizations in which the exciton's emission peak overlaps with the modes' dispersion (marked by white tags in Figure 4a). The similarities between the mode profiles shown in Figure 4b,c to the familiar results from waveguide theory enable the identification of modes of the fabricated asymmetrical waveguiding structure. In our specific case, the relevant modes in the measured angles range are  $TE_2$  and  $TM_1$ . We

notice the field enhancement found within the waveguide upon resonance, another indication of an increase in the local density of optical states. For off-resonance angles, the fields within the waveguiding layer destructively interfere, and negligible values of the normalized electric field are found. The variations in the local density of states alter the isotopically spontaneous emission process of the unoriented NPLs in the waveguide. As a result, emission of photons into guided modes' photonic states becomes favorable, with agreement with our experimental observations.

An important evaluation of the interaction between excitons and optical modes may be given by the variations in emission rate due to the change in emitter's optical environment, i.e. due to the change in available radiative decay channels described by the local density of states. This can be calculated by performing time-correlated single photon counting (TCSPC) measurements of the excitons' lifetime. To measure NPLs' exciton lifetime, the excitation laser beam was divided by a beam splitter (Thorlabs, BS019-30:70), with one arm directed toward a trigger detector (PicoQuant, TDA 200), and the other arm excited the NPLs in the waveguide. The emission was filtered using a band pass filter (Thorlabs, MF510-42-WGFP) and collected by a single photon detector (IDQ, id100T). The two detectors were correlated by the TCSPC system (PicoQuant, Picoharp 300). These measurements were performed for angles where the emission's intensity peaked.

The lifetime measured from the emission leaking out of the waveguide at angles  $43.5^\circ$  and  $49.9^\circ$  (which related to TE and TM mode respectively) presented similar decay rates (see Supporting Information). This observation suggests that the majority of embedded NPLs are simultaneously coupled to all the energetically matching optical modes in the waveguide. This experimentally enables us to combine the results from different angles and increase the signal-to-noise ratio in the lifetime measurements. The combined measurements are presented by the orange dots in Figure 5, together with the blue x's and gray circles which correspond to the original lifetime measurement of NPLs in toluene and a bulk specimen of NPLs in SEBS, respectively (see Supporting Information for the complete lifetime measurements).

The excitons in LHP NPLs' decay in a biexponential trend<sup>43</sup>

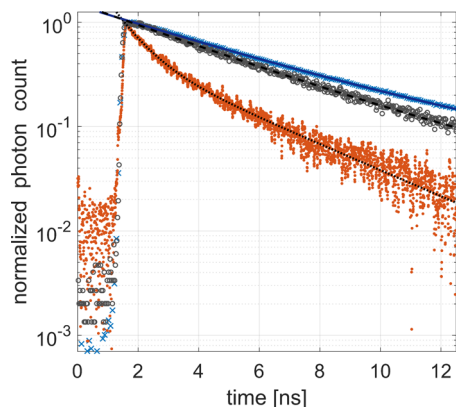


**Figure 5.** Emission lifetime measurements for CsPbBr<sub>3</sub> NPLs activated waveguides (orange), NPL dispersed in toluene (black), NPLs encapsulated in SEBS matrices (blue). Blue line, and black dashed or dotted lines represent the biexponential fit of these measurements (respectively). The fitted lifetime values are in Table 1.

$$I(t) = a_1 e^{-t-t_0/\tau_1} + a_2 e^{-t-t_0/\tau_2} \quad (2)$$

where  $I(t)$  is the photon count,  $t$  represents time,  $t_0$  is the temporal shift, and  $\tau_i$  and  $a_i$  are the lifetime and amplitudes of each exponential term. As each set of measured data was normalized, we used  $a_2 = 1 - a_1$ . In Figure 5 the curves represent the biexponential fit for the presented data, and the fitted lifetimes are gathered in Table 1 (the complete list of fit parameters in Table S1).

**Table 1.** Fitted Lifetimes for the Different NPLs Excitonic Decay Measurements Presented in Figure 5<sup>a</sup>

sample	$\tau_1$ [ns]	$\tau_2$ [ns]
NPL in toluene	$4.44 \pm 0.02$	$13.26 \pm 0.22$
NPLs encapsulated in SEBS matrices	$3.97 \pm 0.05$	$11.7 \pm 0.8$
NPLs activated planar-waveguide	$3.48 \pm 0.08$	$0.82 \pm 0.03$

<sup>a</sup> $\tau_1$  relates to non-radiative decay, and  $\tau_2$ , to radiative decay processes.

In bulk SEBS and toluene, the fast component ( $\tau_1$ ) may relate to nonradiative decay processes.<sup>43</sup> We assume minor differences between the nonradiative processes in similarly made bulk SEBS and the waveguiding samples and then can ascribe the longer lifetime component in the waveguide to the nonradiative process. Focusing on the radiative lifetime ( $\tau_2$ ), we see how placing the NPLs in the waveguide makes it an order of magnitude shorter. We evaluated the Purcell factor using the fitted radiative decay lifetimes for NPLs in SEBS ( $\tau_2^{\text{bulk}}$ ) and the waveguiding slab ( $\tau_2^{\text{wg}}$ )<sup>44</sup>

$$F_p = \frac{\tau_2^{\text{bulk}}}{\tau_2^{\text{wg}}} \approx 14$$

This factor is attributed to the modification of the available radiative decay channels for excitons in the waveguide. While the resulted value is rather moderate for  $F_p$ , evidently it is enough to modify the characteristics of the emitted photons.

In conclusion, we introduced a simple method to fabricate planar optical waveguides activated with LHP NPLs and studied the coupling between the LHP excitons and the optical modes of the waveguide. The NPLs emission shows clear coupling to the optical guided modes, as indicated by emitted photons' momenta and polarization. The coupling to optical modes with specific momenta may be utilized for achieving the desirable directional emission from LHP-based light emitting devices.<sup>45,46</sup> The engineered dielectric environment of the waveguide enables a decrease in the excitons' lifetime by an order of magnitude due to the Purcell effect. Achieving fast emission from perovskite NPLs activated waveguides is of interest in the context of searching for an efficient and coherent single photon source. Further development of the waveguides using state of the art lithography techniques or deposition methods to control the orientation of anisotropic nanoparticles in the polymer<sup>47</sup> is underway. Another goal is to create waveguide–exciton–polaritons hybrid modes. This may be possible even at room temperature when in a strong coupling regime by increasing the density of the NPLs, while retaining the quality of the waveguide<sup>48</sup> as was previously demonstrated with organic dye molecules.<sup>49</sup> These results motivate the use of LHP NCs to activate the waveguide-based system for both fundamental research and future potential applications.

## METHODS

**Nanoplate Synthesis and Characterization.** Cesium oleate solution was prepared prior to the synthesis by taking 0.4 g of  $\text{Cs}_2\text{CO}_3$  and 1.2 mL of OA that were loaded into a three-neck flask along with 15 mL of ODE, they were then degassed under vacuum at 120 °C for 1 h, following a second degassing phase at 150 °C under Ar flow until all  $\text{Cs}_2\text{CO}_3$  reacted with OA. The resulting Cs-oleate was kept in a glovebox as our Cs precursor.

**For the Synthesis of  $\text{CsPbBr}_3$  NPLs.** ODE (5 mL) and  $\text{PbBr}_2$  (0.069 g, 99.999%, Aldrich) were loaded into a 25 mL three-neck flask and dried under vacuum for 1 h at 120 °C. Dried oleylamine (0.5 mL, OLA, Aldrich, 70%) and dried OA (0.5 mL) were injected at 120 °C under Ar. After complete solubilization of a  $\text{PbBr}_2$  salt, the temperature was changed to 130–90 °C, hot (~100 °C) Cs-oleate solution (0.4 mL, 0.125 M in ODE, prepared as described above) was quickly injected, and the reaction mixture was immediately cooled by an ice–water bath.

**Isolation and Characterization of  $\text{CsPbBr}_3$  NPLs.** The NPLs were extracted from the crude solution by centrifuging at 8500 rpm for 5 min. Lower temperature reactions where the crude solution concentration is smaller and thinner NPLs are formed demand longer centrifugation times and cooling the solution to 17 °C (above freezing point of ODE). After centrifugation, the supernatant was discarded, and the particles were redispersed in hexane forming stable colloidal solutions.

The clean NPLs were then characterized via HRTEM (FEI Tecnai at 120 keV), and their absorption and emission properties were measured (BioTek synergy II plate reader).

**Waveguide Fabrication.** The dielectric slab is made by a mixture of NPLs and SEBS (Kraton MD1537). To fabricate the waveguide, SEBS was mixed with toluene to obtain a 12.5% concentration (by weight) and sonicated overnight. Before further use, it was filtered through a nylon syringe filter with a pore size of 0.22  $\mu\text{m}$ . The filtered SEBS–toluene solution was mixed in a 1:3 ratio (favoring the NPLs solution) with toluene containing a high concentration of NPLs (optical density of 0.7 at 400 nm). The mixing process resulted in an unclear solution due to scattering aggregates. Pipette use enabled careful separation of the optically clear solution needed for the formation of the wave-guiding layer from the sunken residues in the bottom of the vial. The substrate used was a 12.7  $\times$  12.7 mm<sup>2</sup> glass slide coated with Indium Tin Oxide (ITO). To form the optical waveguide, the substrate was coated with a 50 nm thick silver layer that was evaporated on top of the ITO coated glass (N-BK7). The ITO serves as an adhesive layer for the silver. The silver was sealed by 2–3 nm of titanium, which upon exposure to air is oxygenated to form a thin protective film of  $\text{TiO}_2$ . The substrate was positioned on a spinner (SCS, P6700) which has been set to accelerate from 0 to 500 rpm in 8 s. During this stage, 85  $\mu\text{L}$  of the clear NPLs-SEBS solution were gradually casted. This casting method has been found to produce a more uniform film with a smaller amount of solution. This stage was followed by a rapid increase to 3500 rpm and retaining this rotation speed for 2 min to form the thin dielectric slab. Finally, the sample was placed in a sealed clean container for about 24 h to fully dry before performing any kind of measurement. These steps produced a submicron waveguiding layer as was measured by a profiler (Veeco, Dektak 6M).

## ASSOCIATED CONTENT

### Supporting Information

The Supporting Information is available free of charge at <https://pubs.acs.org/doi/10.1021/acsphotonics.0c00478>.

Additional reflection and emission measurements performed on 3-unit-cells thick NPLs; complete lifetime plot and a table containing biexponential decay fit parameters, in toluene and from waveguide at different angles (PDF)

## AUTHOR INFORMATION

### Corresponding Author

**Yehonadav Bekenstein** – Department of Materials Science and Engineering and the Solid-State Institute, Technion – Israel Institute of Technology, 32000 Haifa, Israel; [orcid.org/0000-0001-6230-5182](https://orcid.org/0000-0001-6230-5182); Email: [bekenstein@technion.ac.il](mailto:bekenstein@technion.ac.il)

### Authors

**Tsafrir Abir** – Department of Condensed Matter Physics, School of Physics and Astronomy, Tel Aviv University, Tel Aviv 69978, Israel; Department of Physical Electronics, School of Electrical Engineering, Tel-Aviv University, Tel Aviv 69978, Israel;

[orcid.org/0000-0002-6609-3655](https://orcid.org/0000-0002-6609-3655)

**Reut Shechter** – Department of Materials Science and Engineering and the Solid-State Institute, Technion – Israel Institute of Technology, 32000 Haifa, Israel

**Tal Ellenbogen** – Department of Physical Electronics, School of Electrical Engineering, Tel-Aviv University, Tel Aviv 69978, Israel

Complete contact information is available at:

<https://pubs.acs.org/doi/10.1021/acsphotonics.0c00478>

### Notes

The authors declare no competing financial interest.

## ACKNOWLEDGMENTS

The authors thank A. P. Alivisatos and UC Berkeley for their generosity in supplying the physical support that has enabled this collaboration. This collaboration was initiated through funding from the 2017 Raymond and Beverly Sackler Fund for Convergence Research in Biomedical, Physical and Engineering Sciences. T.E. and T.A. thank the Israel Ministry of Science and Technology for their generous support. Y.B. and R.S. thank the Hellen Diller quantum center and the Nancy and Stephen Grand Technion energy program, for their generous support of our new group. Y.B. thanks the Irwin and Bethea Green and Detroit chapter career advancement chair and the Alon program. We thank Orr Beer for proofreading the manuscript.

## REFERENCES

- (1) Sutherland, B. R.; Sargent, E. H. Perovskite Photonic Sources. *Nat. Photonics* **2016**, *10*, 295–302.
- (2) Kagan, C. R.; Mitzi, D. B.; Dimitrakopoulos, C. D. Organic-Inorganic Hybrid Materials as Semiconducting Channels in Thin-Film Field-Effect Transistors. *Science* **1999**, *286*, 945–947.
- (3) Lee, M. M.; Teuscher, J.; Miyasaka, T.; Murakami, T. N.; Snaith, H. J. Efficient Hybrid Solar Cells Based on Meso-Superstructured Organometal Halide Perovskites. *Science* **2012**, *338*, 643–647.
- (4) Tan, Z. K.; Moghaddam, R. S.; Lai, M. L.; Docampo, P.; Higler, R.; Deschler, F.; Price, M.; Sadhanala, A.; Pazos, L. M.; Credgington, D.; et al. Bright Light-Emitting Diodes Based on Organometal Halide Perovskite. *Nat. Nanotechnol.* **2014**, *9*, 687–692.

- (5) Lin, K.; Xing, J.; Quan, L. N.; de Arquer, F. P. G.; Gong, X.; Lu, J.; Xie, L.; Zhao, W.; Zhang, D.; Yan, C.; et al. Perovskite Light-Emitting Diodes with External Quantum Efficiency Exceeding 20 per Cent. *Nature* **2018**, *562*, 245–248.
- (6) Kovalenko, M. V.; Protesescu, L.; Bodnarchuk, M. I. Properties and Potential Optoelectronic Applications of Lead Halide Perovskite Nanocrystals. *Science* **2017**, *358*, 745–750.
- (7) Akkerman, Q. A.; Rainò, G.; Kovalenko, M. V.; Manna, L. Genesis, Challenges and Opportunities for Colloidal Lead Halide Perovskite Nanocrystals. *Nat. Mater.* **2018**, *17*, 394–405.
- (8) Shamsi, J.; Urban, A. S.; Imran, M.; De Trizio, L.; Manna, L. Metal Halide Perovskite Nanocrystals: Synthesis, Post-Synthesis Modifications, and Their Optical Properties. *Chem. Rev.* **2019**, *119*, 3296–3348.
- (9) Bekenstein, Y.; Koscher, B. A.; Eaton, S. W.; Yang, P.; Alivisatos, A. P. Highly Luminescent Colloidal Nanoplates of Perovskite Cesium Lead Halide and Their Oriented Assemblies. *J. Am. Chem. Soc.* **2015**, *137*, 16008–16011.
- (10) Koscher, B. A.; Swabeck, J. K.; Bronstein, N. D.; Alivisatos, A. P. Essentially Trap-Free CsPbBr<sub>3</sub> Colloidal Nanocrystals by Postsynthetic Thiocyanate Surface Treatment. *J. Am. Chem. Soc.* **2017**, *139*, 6566–6569.
- (11) Zhang, Q.; Ha, S. T.; Liu, X.; Sum, T. C.; Xiong, Q. Room-Temperature near-Infrared High-Q Perovskite Whispering-Gallery Planar Nanolasers. *Nano Lett.* **2014**, *14*, 5995–6001.
- (12) Ha, S. T.; Liu, X.; Zhang, Q.; Giovanni, D.; Sum, T. C.; Xiong, Q. Synthesis of Organic-Inorganic Lead Halide Perovskite Nanoplatelets: Towards High-Performance Perovskite Solar Cells and Optoelectronic Devices. *Adv. Opt. Mater.* **2014**, *2*, 838–844.
- (13) Liu, J.; Chen, K.; Khan, S. A.; Shabbir, B.; Zhang, Y.; Khan, Q.; Bao, Q. Synthesis and Optical Applications of Low Dimensional Metal-Halide Perovskites. *Nanotechnology* **2020**, *31*, 152002.
- (14) Gu, Z.; Zhou, Z.; Huang, Z.; Wang, K.; Cai, Z.; Hu, X.; Li, L.; Li, M.; Zhao, Y. S.; Song, Y. Controllable Growth of High-Quality Inorganic Perovskite Microplate Arrays for Functional Optoelectronics. *Adv. Mater.* **2020**, *32*, 1908006.
- (15) Zhang, Q.; Su, R.; Liu, X.; Xing, J.; Sum, T. C.; Xiong, Q. High-Quality Whispering-Gallery-Mode Lasing from Cesium Lead Halide Perovskite Nanoplatelets. *Adv. Funct. Mater.* **2016**, *26*, 6238–6245.
- (16) Su, R.; Ghosh, S.; Wang, J.; Liu, S.; Diederichs, C.; Liew, T. C. H.; Xiong, Q. Observation of Exciton Polariton Condensation in a Perovskite Lattice at Room Temperature. *Nat. Phys.* **2020**, *16*, 301–306.
- (17) Di, X.; Hu, Z.; Jiang, J.; He, M.; Zhou, L.; Xiang, W.; Liang, X. Use of Long-Term Stable CsPbBr<sub>3</sub> Perovskite Quantum Dots in Phospho-Silicate Glass for Highly Efficient White LEDs. *Chem. Commun.* **2017**, *53*, 11068–11071.
- (18) Raja, S. N.; Bekenstein, Y.; Koc, M. A.; Fischer, S.; Zhang, D.; Lin, L.; Ritchie, R. O.; Yang, P.; Alivisatos, A. P. Encapsulation of Perovskite Nanocrystals into Macroscale Polymer Matrices: Enhanced Stability and Polarization. *ACS Appl. Mater. Interfaces* **2016**, *8*, 35523–35533.
- (19) Zhang, X.; Sun, C.; Zhang, Y.; Wu, H.; Ji, C.; Chuai, Y.; Wang, P.; Wen, S.; Zhang, C.; Yu, W. W. Bright Perovskite Nanocrystal Films for Efficient Light-Emitting Devices. *J. Phys. Chem. Lett.* **2016**, *7*, 4602.
- (20) Chiba, T.; Hoshi, K.; Pu, Y. J.; Takeda, Y.; Hayashi, Y.; Ohisa, S.; Kawata, S.; Kido, J. High-Efficiency Perovskite Quantum-Dot Light-Emitting Devices by Effective Washing Process and Interfacial Energy Level Alignment. *ACS Appl. Mater. Interfaces* **2017**, *9*, 18054–18060.
- (21) Li, J.; Xu, L.; Wang, T.; Song, J.; Chen, J.; Xue, J.; Dong, Y.; Cai, B.; Shan, Q.; Han, B.; et al. 50-Fold EQE Improvement up to 6.27% of Solution-Processed All-Inorganic Perovskite CsPbBr<sub>3</sub> QLEDs via Surface Ligand Density Control. *Adv. Mater.* **2017**, *29*, 1603885.
- (22) Swarnkar, A.; Marshall, A. R.; Sanehira, E. M.; Chernomordik, B. D.; Moore, D. T.; Christians, J. A.; Chakrabarti, T.; Luther, J. M. Quantum Dot-Induced Phase Stabilization of  $\alpha$ -CsPbI<sub>3</sub> Perovskite for High-Efficiency Photovoltaics. *Science* **2016**, *354*, 92–95.
- (23) Akkerman, Q. A.; Gandini, M.; Di Stasio, F.; Rastogi, P.; Palazon, F.; Bertoni, G.; Ball, J. M.; Prato, M.; Petrozza, A.; Manna, L. Strongly Emissive Perovskite Nanocrystal Inks for High-Voltage Solar Cells. *Nat. Energy* **2017**, *2*, 16194.
- (24) Yakunin, S.; Protesescu, L.; Krieg, F.; Bodnarchuk, M. I.; Nedelcu, G.; Humer, M.; De Luca, G.; Fiebig, M.; Heiss, W.; Kovalenko, M. V. Low-Threshold Amplified Spontaneous Emission and Lasing from Colloidal Nanocrystals of Caesium Lead Halide Perovskites. *Nat. Commun.* **2015**, *6*, 8056.
- (25) Wang, Y.; Li, X.; Song, J.; Xiao, L.; Zeng, H.; Sun, H. All-Inorganic Colloidal Perovskite Quantum Dots: A New Class of Lasing Materials with Favorable Characteristics. *Adv. Mater.* **2015**, *27*, 7101–7108.
- (26) Becker, M. A.; Vaxenburg, R.; Nedelcu, G.; Sercel, P. C.; Shabaev, A.; Mehl, M. J.; Michopoulos, J. G.; Lambrakos, S. G.; Bernstein, N.; Lyons, J. L.; et al. Bright Triplet Excitons in Caesium Lead Halide Perovskites. *Nature* **2018**, *553*, 189–193.
- (27) Rainò, G.; Nedelcu, G.; Protesescu, L.; Bodnarchuk, M. I.; Kovalenko, M. V.; Mahrt, R. F.; Stöferle, T. Single Cesium Lead Halide Perovskite Nanocrystals at Low Temperature: Fast Single-Photon Emission, Reduced Blinking, and Exciton Fine Structure. *ACS Nano* **2016**, *10*, 2485.
- (28) Park, Y. S.; Guo, S.; Makarov, N. S.; Klimov, V. I. Room Temperature Single-Photon Emission from Individual Perovskite Quantum Dots. *ACS Nano* **2015**, *9*, 10386–10393.
- (29) Utzat, H.; Sun, W.; Kaplan, A. E. K.; Krieg, F.; Ginterseder, M.; Spokoyny, B.; Klein, N. D.; Shulenberg, K. E.; Perkinson, C. F.; Kovalenko, M. V.; et al. Coherent Single Photon Emission from Colloidal Lead Halide Perovskite Quantum Dots. *Science* **2019**, *363*, 1068–1072.
- (30) Shoaib, M.; Wang, X.; Zhang, X.; Wang, X.; Zhou, H.; Xu, T.; Hu, X.; Liu, H.; Fan, X.; Zheng, W.; et al. Directional Growth of Ultralong CsPbBr<sub>3</sub> Perovskite Nanowires for High-Performance Photodetectors. *J. Am. Chem. Soc.* **2017**, *139*, 15592–15595.
- (31) Chen, J.; Fu, Y.; Samad, L.; Dang, L.; Zhao, Y.; Shen, S.; Guo, L.; Jin, S. Vapor-Phase Epitaxial Growth of Aligned Nanowire Networks of Cesium Lead Halide Perovskites (CsPbX<sub>3</sub>, X = Cl, Br, I). *Nano Lett.* **2017**, *17*, 460–466.
- (32) Oksenberg, E.; Sanders, E.; Popovitz-Biro, R.; Houben, L.; Joselevich, E. Surface-Guided CsPbBr<sub>3</sub> Perovskite Nanowires on Flat and Faceted Sapphire with Size-Dependent Photoluminescence and Fast Photoconductive Response. *Nano Lett.* **2018**, *18*, 424–433.
- (33) Wang, X.; Shoaib, M.; Wang, X.; Zhang, X.; He, M.; Luo, Z.; Zheng, W.; Li, H.; Yang, T.; Zhu, X.; et al. High-Quality In-Plane Aligned CsPbX<sub>3</sub> Perovskite Nanowire Lasers with Composition-Dependent Strong Exciton-Photon Coupling. *ACS Nano* **2018**, *12*, 6170–6178.
- (34) Zhu, H.; Fu, Y.; Meng, F.; Wu, X.; Gong, Z.; Ding, Q.; Gustafsson, M. V.; Trinh, M. T.; Jin, S.; Zhu, X. Y. Lead Halide Perovskite Nanowire Lasers with Low Lasing Thresholds and High Quality Factors. *Nat. Mater.* **2015**, *14*, 636–642.
- (35) Fu, Y.; Zhu, H.; Stoumpos, C. C.; Ding, Q.; Wang, J.; Kanatzidis, M. G.; Zhu, X.; Jin, S. Broad Wavelength Tunable Robust Lasing from Single-Crystal Nanowires of Cesium Lead Halide Perovskites (CsPbX<sub>3</sub>, X = Cl, Br, I). *ACS Nano* **2016**, *10*, 7963–7972.
- (36) Suárez, I.; Hassanabadi, E.; Maulu, A.; Carlino, N.; Maestri, C. A.; Latifi, M.; Bettotti, P.; Mora-Seró, I.; Martínez-Pastor, J. P. Integrated Optical Amplifier-Photodetector on a Wearable Nanocellulose Substrate. *Adv. Opt. Mater.* **2018**, *6*, 1–8.
- (37) Suárez, I.; Juárez-Pérez, E. J.; Bisquert, J.; Mora-Seró, I.; Martínez-Pastor, J. P. Polymer/Perovskite Amplifying Waveguides for Active Hybrid Silicon Photonics. *Adv. Mater.* **2015**, *27*, 6157–6162.
- (38) Li, Y. J.; Lv, Y.; Zou, C. L.; Zhang, W.; Yao, J.; Zhao, Y. S. Output Coupling of Perovskite Lasers from Embedded Nanoscale Plasmonic Waveguides. *J. Am. Chem. Soc.* **2016**, *138*, 2122–2125.
- (39) Cegielski, P. J.; Neutzner, S.; Porschatis, C.; Lerch, H.; Bolten, J.; Suckow, S.; Kandada, A. R. S.; Chmielak, B.; Petrozza, A.;

Wahlbrink, T.; et al. Integrated Perovskite Lasers on a Silicon Nitride Waveguide Platform by Cost-Effective High Throughput Fabrication. *Opt. Express* **2017**, *25*, 13199.

(40) Weidman, M. C.; Goodman, A. J.; Tisdale, W. A. Colloidal Halide Perovskite Nanoplatelets: An Exciting New Class of Semiconductor Nanomaterials. *Chem. Mater.* **2017**, *29*, 5019–5030.

(41) Rainò, G.; Landuyt, A.; Krieg, F.; Bernasconi, C.; Ochsenbein, S. T.; Dirin, D. N.; Bodnarchuk, M. I.; Kovalenko, M. V. Underestimated Effect of a Polymer Matrix on the Light Emission of Single CsPbBr<sub>3</sub> Nanocrystals. *Nano Lett.* **2019**, *19*, 3648–3653.

(42) Ohta, K.; Ishida, H. Matrix Formalism for Calculation of Electric Field Intensity of Light in Stratified Multilayered Films. *Appl. Opt.* **1990**, *29*, 1952–1959.

(43) Bohn, B. J.; Tong, Y.; Gramlich, M.; Lai, M. L.; Döblinger, M.; Wang, K.; Hoye, R. L. Z.; Müller-Buschbaum, P.; Stranks, S. D.; Urban, A. S.; et al. Boosting Tunable Blue Luminescence of Halide Perovskite Nanoplatelets through Postsynthetic Surface Trap Repair. *Nano Lett.* **2018**, *18*, 5231–5238.

(44) Novotny, L.; Hecht, B. *Principles of Nano-Optics*; Cambridge University Press: 2012; Vol. 9781107005.

(45) Walters, G.; Haeberlé, L.; Quintero-Bermudez, R.; Brodeur, J.; Kéna-Cohen, S.; Sargent, E. H. Directional Light Emission from Layered Metal Halide Perovskite Crystals. *J. Phys. Chem. Lett.* **2020**, *11*, 3458–3465.

(46) Jurow, M. J.; Morgenstern, T.; Eisler, C.; Kang, J.; Penzo, E.; Do, M.; Engelmayer, M.; Osowiecki, W. T.; Bekenstein, Y.; Tassone, C.; et al. Manipulating the Transition Dipole Moment of CsPbBr<sub>3</sub> Perovskite Nanocrystals for Superior Optical Properties. *Nano Lett.* **2019**, *19*, 2489–2496.

(47) Zhou, N.; Bekenstein, Y.; Eisler, C. N.; Zhang, D.; Schwartzberg, A. M.; Yang, P.; Alivisatos, A. P.; Lewis, J. A. Perovskite Nanowire-Block Copolymer Composites with Digitally Programmable Polarization Anisotropy. *Sci. Adv.* **2019**, *5*, No. eaav8141.

(48) Eizner, E.; Avayu, O.; Ditcovski, R.; Ellenbogen, T. Aluminum Nanoantenna Complexes for Strong Coupling between Excitons and Localized Surface Plasmons. *Nano Lett.* **2015**, *15*, 6215–6221.

(49) Ellenbogen, T.; Crozier, K. B. Exciton-Polariton Emission from Organic Semiconductor Optical Waveguides. *Phys. Rev. B: Condens. Matter Mater. Phys.* **2011**, *84*, 161304.